International Journal of Multiphysics
Volume 18, No. 2, 2024
ISSN: 1750-9548

Research on the Identification Method of Slice Images of Tight Oil Reservoir Rocks Based on Improved Refine Mask

Zihao Mu[1*], Chunsheng Li[1], Zongbao Liu[2], Tao Liu[1],Kejia Zhang[1],Yuchen Yang[2]

[1] School of Computer & Information Technology, Northeast Petroleum University, Daqing 163319

[2] School of Earth Sciences, Northeast Petroleum University, Daqing 163319

*Corresponding Author: Zihao Mu .15701219426@163.com

Abstract: Terrestrial tight oil exhibits strong diagenetic heterogeneity, and a large number of rock slices are required to reveal the true micro-pore throat structure characteristics. Traditional identification methods for tight oil rock slices suffer from long manual observation time, poor accuracy of machine learning method and strong subjectivity of manual judgment, making it difficult to meet the requirements of reservoir fine description and quantitative characterization. In this study, targeting the Upper Paleozoic in the North Subsag Basin of China and the Linxing Block of Ordos Basin, a deep learning-based identification method for slice features of tight oil reservoir rocks was proposed. Firstly, the image preprocessing technique was investigated and the Gaussian denoising filtering algorithm was applied to reasonably allocate Gaussian weight coefficients to the original images, ensuring the quality of the samples. Secondly, the self-labeling image data augmentation technique was constructed to address the problem of sparse samples. Thirdly, the RefineMask instance segmentation algorithm was introduced and improved to simultaneously achieve segmentation and identification of components in slices of tight oil reservoir rocks. Finally, the experiment demonstrates that the SLA-RefineMask method has significant advantages in terms of accuracy and execution speed compared to other methods.

Keywords: tight oil reservoir; rock slice; feature identification; instance segmentation; unconventional oil and gas

1. Introduction

With the increasing global energy demand and rapid development of unconventional oil and gas exploration and extraction technologies, the importance of unconventional oil and gas production, particularly tight oil, has been steadily rising, and accurate evaluation of the micro-pore structure in tight sandstone is crucial for enhancing the accuracy of reservoir evaluation and the standard of diagenetic facies[1]. Tight sandstone reservoirs have

undergone complex geological processes and tectonic modifications over an extensive period, resulting in lithological tightness, small pore size, narrow throats, poor pore-throat connectivity and high heterogeneity[2]. The automatic particle segmentation of tight sandstone is to divide mineral particles into distinct regions on slices, which is the initial step in computer-aided mineral identification and sandstone classification. However, the presence of numerous mineral particles and the indistinct boundaries between neighboring quartz, feldspar and lithics in the microscopic image of tight sandstone pose significant challenges for particle segmentation[3]. Current approaches have drawbacks such as time-consuming manual observation, limited accuracy of machine learning method and subjective human judgment, and the deep learning-based slice identification technology of tight sandstone faces many challenges[4].

Existing methods for slice segmentation and rapid identification of tight oil reservoir rocks are susceptible to noise interference, inadequate algorithm design, complexity of image structures and other factors, resulting in low segmentation and identification accuracy. Moreover, the intricate and costly process of preparing slices of tight oil reservoir rocks leads to a persistent shortage of samples in these methods. To address the intelligent identification of slices of tight sandstone rocks, extensive research has been conducted by scholars worldwide, yielding significant research findings. Based on segmentation characteristics and processing granularity, deep learning-based image segmentation of slices of tight oil reservoir rocks can be classified into two major categories: superpixel segmentation method[5] and instance segmentation method[6]. The superpixel segmentation method can be further divided into graph theory method and pixel clustering method. While the graph theory normalized segmentation method proposed by Yang Dandan et al.[7] exhibits certain advantages over traditional segmentation methods in mineral particle segmentation, it tends to suffer from over-segmentation. Liu Ye et al.[8] applied the K-means clustering algorithm based on simple linear iteration to rock image segmentation and identification. Although this method achieved basic automation of component identification under conditions of minimal data differences, it caused great difficulties for the subsequent process due to the gaps in rock slice images. Instance segmentation, which combines object detection and semantic segmentation algorithms, has been explored by Jiang Feng et al.[9], who utilized the idea of semantic segmentation to extract particle information from sandstone slice images. However, challenges remain in optimizing network structures, setting hyperparameters, etc. Lei Mingfeng et al.[10] employed the Mask R-CNN instance segmentation method based on deep learning to achieve intelligent detection and quantification of mineral particles in rock slices. However, the Mask R-CNN algorithm sacrifices some detail information during instance segmentation, leading to inaccurate identification.

In recent years, deep learning-based object detection algorithms have developed rapidly[11] and have been widely applied in various fields, including vehicle detection in traffic scene[12], object detection in remote sensing images in the aerial and satellite image analysis[13], and automatic segmentation of brain CT images in the medical field[14]. However, their application to mineral detection in rock slices remains limited. Therefore, based on a contrastive analysis of several prevalent object detection algorithms, the RefineMask deep learning algorithm[15] was selected and improved, and a self-labeling augmented RefineMask method for component

identification of tight oil slices based on transfer learning (SLA-RefineMask) was proposed for high-quality object and scene instance segmentation. Firstly, the Gaussian denoising filtering algorithm was applied to remove image noise and unify pixel sizes, ensuring high-quality sample images. Secondly, to address the issue of limited sample quantity, a self-labeling image data augmentation mechanism was designed. Subsequently, the RefineMask algorithm was introduced and improved to achieve simultaneous segmentation and identification of components in tight oil rock slices. Finally, through experimental validation, the improved SLA-RefineMask method demonstrates significant advantages in terms of segmentation accuracy, identification effectiveness and running speed compared to previous methods.

2. SLA-RefineMask Method

The study process of this paper mainly includes the establishment of slice image data set, augmentation of slice images and identification of slice image components. The establishment of the slice data set involves the application of image preprocessing technique, while the augmentation of slice images utilizes a self-labeling image augmentation mechanism. The key to the identification of slice image components lies in the SLA-RefineMask algorithm. The following sections will discuss in detail the augmentation of slice images based on the self-labeling mechanism to achieve the augmentation of a few labeled images. The precise segmentation and identification of slice image components is achieved with the SLA-RefineMask algorithm.

2.1 Establishment of slice image data set

To ensure sufficient training samples for slice component identification, the tight sandstone casting slice image data set needs to be established. In this study, two target regions in China, namely the Upper Paleozoic of Linxing Block in Ordos Basin (OB data set) and the North Subsag (NT data set), were used as the original data sets, with a total of 100 bitmap images. The OB data set is a self-made pixel data set with an original image size of 2560 pixels * 1920 pixels, which is a migration test data set with 50 samples; while the NT data set is a migration test data set with an original size of 768 pixels * 567 pixels, which consists of 50 samples.

First, the images were preprocessed. How to effectively remove filter noise while preserving the edge and texture details of the images has been a vital technical issue in the field of digital image processing[16-18]. Since the Non-regular Area Gaussian Filtering algorithm [19] can preserve the texture features of the images while filtering, it was first used to achieve image denoising. This algorithm analyzes the texture autocorrelation characteristics and constructs local irregular autocorrelation regions to eliminate possible noise or pixels with low correlation, thereby improving the rationality of weight coefficient allocation based on Gaussian filtering. The local irregular Gaussian mask region is built based on the analysis of grayscale similarity. Therefore, by combining it with the traditional Gaussian filtering algorithm, the local spatial distance and texture correlation can be comprehensively considered, and Gaussian mask Windows of different shapes can be adaptively selected for different texture feature regions to allocate Gaussian weight coefficients reasonably, as shown in Equation (1):

$$I_{ngf}(x, y)=\frac{\sum_{(i, j)\in\Omega_{x, y}} w_d(i, j)\, I(i, j)}{\sum_{(i, j)\in\Omega_{x, y}} w_d(i, j)} \tag{1}$$

Where, $W_{x, y}$ represents the local irregular Gaussian mask region, and meets $W_{x, y}$ ï $w_{x, y}$, and the specific implementation algorithm of Gaussian filtering based on the irregular region proposed in this paper is shown below.

Algorithm 1 Gaussian filtering based on the irregular region

Input: Input image I, similarity weight allocation x, radius r, similarity threshold:

Output: Filtered image I_{ngf}

For $I(x, y)$ from I (½¤2½¤2½ to $I(I_{width}$ ¾¤2½, I_{height} ¾¤2½

(1) Calculate the local arm length feature $\{h_p^0, h_p^1, h_p^2, h_p^3\}$ of I from the similarity reference function and the arm length feature of the local autocorrelation irregular region;

(2) Construct the local irregular Gaussian mask region Wp.

(3) Realize Gaussian convolution by Equation (1) to get I_{ngf}.

End For

Image labeling aims to guide the training process to achieve the desired results. Professionals study selected images of tight oil reservoirs and use the Labelme software to annotate the image data set into seven types: Quartz, Feldspar, Lithic, Primary Pore (PP), Casting Pore (CP), Cemented Dissolution Pore (CDP), and Microcrack. The labeled image samples will form JSON files and be converted to the desired format.

2.2 Augmentation of slice images

With the deepening of model network layer in deep learning, there is a significant increase in the demand for network training labeled sample data sets. However, due to the high cost of data annotation, it is often challenging to meet this demand in many practical applications. To address the high annotation cost in identifying rock tight oil slices, the self-labeling image augmentation mechanism[20,21] was employed in this study to expand the data set size and improve network robustness and generalization. The self-labeling mechanism was introduced for SLA-RefineMask based on the image processing technique to augment the labeled image samples and their corresponding labeled files. To ensure the clarity of augmented images and the accuracy of labeling points, this algorithm employs four image augmentation techniques through the data

enhancement method of digital image processing[22], including flipping, random cropping[23], noise addition[24] and image blending[25]. The noise intensity was estimated to address the problem of noise pollution in tight sandstone slice images. Then, the adaptive median filtering was performed with an appropriate filter window based on the estimated noise intensity to remove stripe noise and impulse noise[26]. Furthermore, the weight function was modified based on the noise intensity, and most of the noise was removed by improved non-local mean filtering, achieving better denoising results.

(1) Flipping: Horizontal mirror flipping, vertical mirror flipping and diagonal mirror flipping of the images.

(2) Random cropping: Scale the short side of all images to a resolution of 224 pixels and the long side to the same scale, and randomly crop a 224×224 pixel region from the scaled image. The training data obtained by random clipping effectively improves the accuracy of rock slice classification.

(3) Noise addition: Apply noise addition operations to the global, horizontal, vertical and diagonal directions of the tight sandstone slice images with noise percentages of 0.05, 0.075, 0.1 and 0.125.

(4) Image blending: Implementing a combination of operations such as rotation (rotation angles of 45 degrees and 90 degrees), zooming (scaling ratios of 0.6 and 1.5) and shifting (shift amplitudes of 0.1 and 0.2) on the tight sandstone slice images, to generate additional 9 augmented images for each image. Then, carry out the combination operation by means of image blurring with different convolution kernels and an x-axis standard deviation of 5, to generate additional 16 augmented images for each image.

The augmented sample size is 5000 images, which are divided into data set and test set in an 8:2 ratio to meet the requirements of model training. A rich and accurate data set of tight sandstone slices was successfully constructed using the above method, which provides a reliable basis for subsequent experiments and analysis.

2.3 Identification of slice image components

In general, different mineral particles in sandstone images have similar characteristics and blurry boundaries, and the sandstone mineral particles contain relatively complex crystal microstructure, such as cleavage, fracture and twin crystals, which are often misjudged as particle boundaries during the segmentation process, leading to erroneous results. Therefore, this study embeds the attention mechanism[27] into the feature extraction network of the model to improve mineral identification accuracy and segmentation precision. The channel attention mechanism was embedded into the improved RefineMask algorithm, which can be implemented in three steps: First, modifying the pre-trained network structure based on component types; Secondly, optimizing the pre-trained network with a smaller learning rate; Finally, completing the algorithm training to realize component segmentation and identification.

An Attention Based Multi-Scale Feature Fusion Module (AMFF) was designed in the middle layer of the network in this study. The features at each position were selectively aggregated through the weighted sum of the features of the first two layers and the last encoding layer, and similar features were correlated with each other.

In the decoder part, the attention mechanism was applied to preserve gap details for the upsampling features and the corresponding encoding layer features through the Fusion Optimization (FO) module designed by us, while expanding the receptive field with dilated convolutions, ensuring both the integrity and continuity of gap detection. The identification core of slice image components was applied to the RefineMask framework. The SLA-RefineMask algorithm consists of five parts: backbone extraction network, semantic head branch, mask head branch, boundary-aware refinement, training and inference.

(1) Based on the FPN[28] object detector, RefineMask includes two small network modules: the Semantic Head and the Mask Head. The Semantic Head branch uses the highest-resolution feature map in the FPN as input and does not include spatial compression operations such as downsampling. Therefore, the output of the Semantic Head branch has the same size as the input, ensuring rich detailed information in the output. The output of the Semantic Head branch is used to assist the Mask Head branch in instance segmentation. The Mask Head branch completes the instance segmentation task in a "multi-stage" manner, and each stage includes the Semantic Fusion Module (SFM). The Mask Head branch fuses semantic features and semantic masks containing fine-grained information, and then increases the feature map size for more fine-grained mask prediction. Additionally, the Mask Head branch includes the Boundary-Aware Refinement (BAR) operation to enhance the prediction capability of instance boundaries, as shown in Figure 1.

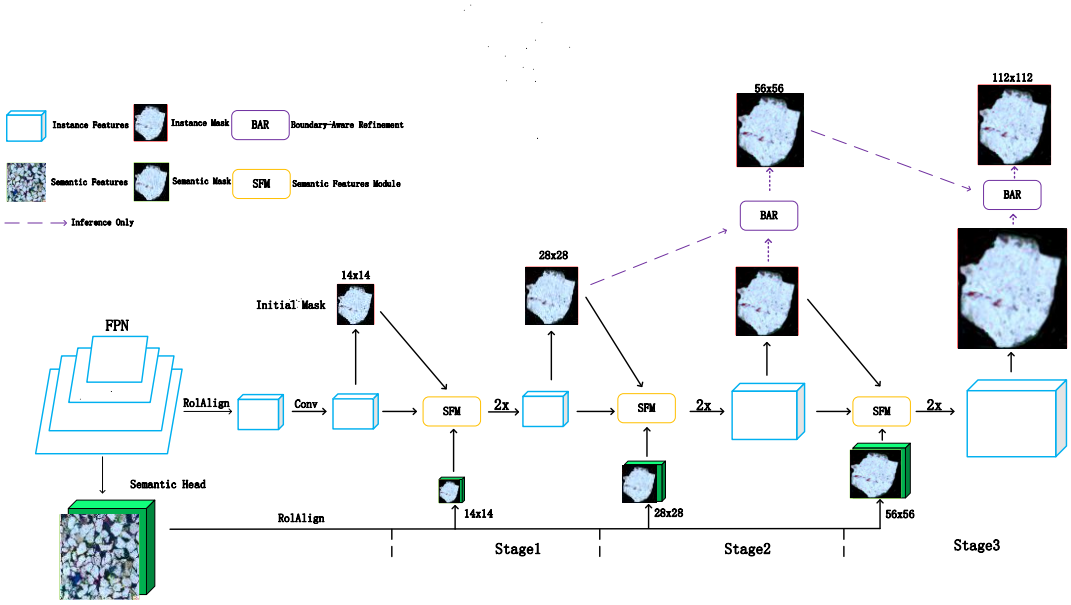

Figure 1. Workflow of the SLA-RefineMask identification method

(2) The Semantic Head branch consists of four convolutional layers for extracting semantic information from the entire input image. It also includes a binary classifier for predicting the probability of each pixel belonging to the foreground, and predicting the high-resolution semantic mask for the entire image under the supervision of the binary cross-entropy loss function. Fine-grained features are further used to supplement the details lost in

the mask branch and obtain high-quality mask prediction.

(3) The main operation in the Mask Head branch is a multi-level refinement process, where each stage involves four inputs: (1) instance features, (2) instance mask, (3) semantic features, and (4) semantic mask. In each stage, the Semantic Fusion Module (SFM) fuses the four inputs and then performs upsampling to obtain larger-sized features. The SFM structure is illustrated in Figure 2. SFM starts with a convolution operation to fuse the multiple inputs and reduce the number of channels. It is followed by three parallel convolutions, each with different dilation parameters to extract features with different receptive fields. Finally, the instance mask, semantic mask and fused features are subject to concat operation to serve as the output of SFM.

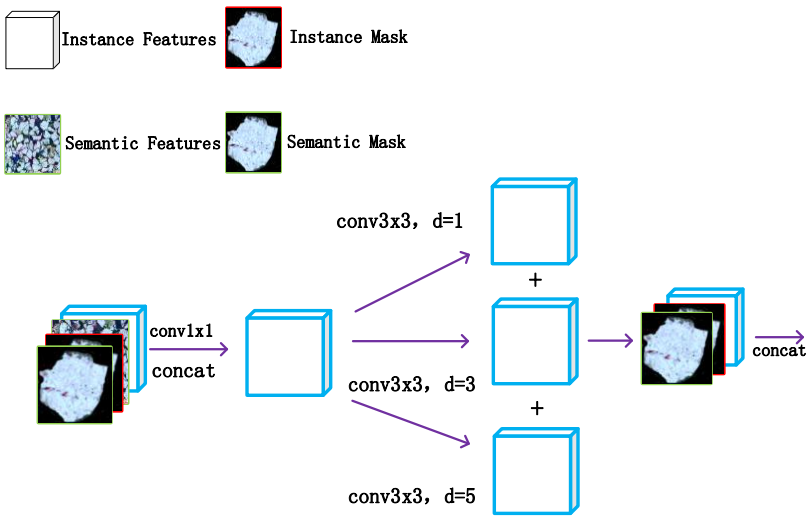

Figure 2. SFM structure diagram

(4) Boundary-Aware Refinement process. M^{k} is used to represent the instance mask branch of the K-th stage, and the size of M^{k} is $4\cdot 2^{k}$ ′ $4\cdot 2^{k}$, where k =1,2,3. B^{k} is used to represent the boundary region of M_{k}, and the definition of B^{k} is shown in Equation (2):

$$B_{k}(i,j)=\begin{cases}1, if & d_{ij}\le d¢\\ 0, & otherwise.\end{cases} \tag{2}$$

Where, (i,j) represents the position of pixel p_{ij} in M^{k}, and d_{ij} represents the Euclidean distance from p_{ij} to M_{k} boundary. The mask boundary is shown in Figure 3 below. For fast calculation, the author uses convolution operation for approximate solution. If the boundary width is 1, the convolution kernel is shown in

Equation (3) :

$$\begin{pmatrix} -1 & -1 & -1 \\ -1 & 8 & -1 \\ -1 & -1 & -1 \end{pmatrix} \tag{3}$$

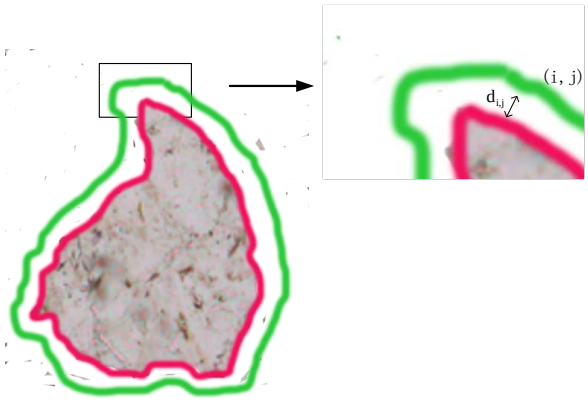

Figure 3. Object boundary region

If the boundary width is 2, the convolution kernel can be obtained by Equation (4):

$$\begin{bmatrix} -1 & -1 & -1 & -1 & -1 \\ -1 & -1 & -1 & -1 & -1 \\ -1 & -1 & 24 & -1 & -1 \\ -1 & -1 & -1 & -1 & -1 \\ -1 & -1 & -1 & -1 & -1 \end{bmatrix} \tag{4}$$

The above convolution kernel is applied to M_k, and the output result is denoted as D_k, which has the same size as M_k. B_k can be calculated by Equation (5):

$$B_k(i,j) = \begin{cases} 1, & \text{if } D^k(i,j) > 0 \\ 0, & otherwise \end{cases} \tag{5}$$

The width of the boundary region is set to 2 during training and 1 during inference.

(5) Training and inference process. Training process: In the multiple branches of the mask head, except for the first stage, the instance segmentation of the other stages only contains the information of the boundary region. Their loss functions during training are represented by Equations (6), (7) and (8):

$$L^k = \frac{1}{d_n} \sum_{n=0}^{N-1} \sum_{i=0}^{S_k-1} \sum_{j=0}^{S_k-1} R_{nij}^k * l_{nij} \tag{6}$$

$$R^k = f_{up}(B_G^{k-1} \cup B_P^{k-1}) \tag{7}$$

$$d_n = \sum_{n=0}^{N-1} \sum_{i=0}^{S_k-1} \sum_{j=0}^{S_k-1} R_{nij} \tag{8}$$

R_k in the loss function represents the bilinear upsampling of the union of the boundary regions of the manually annotated box and the predicted annotated box in the previous stage, L_{nij} is the binary cross entropy loss of the n-th instance at position (i, j), N is the number of instances, and $S_k \times S_k$ is the size of the output feature in the k-th stage. Inference process: The final output of each stage during inference is shown in Equations (9) and (10):

$$M^{k-1} = M^1 \tag{9}$$

$$M^{k} = f_{up}(B_P^{k-1}) \otimes M^k + (1 - f_{up}(B_P^{k-1})) \otimes f_{up}(M^{k-1}) \tag{10}$$

Where, $\otimes$ represents pixel-level multiplication. Figure 4 shows the inference process in the second stage, which is trained and repeated until the best mask is obtained.

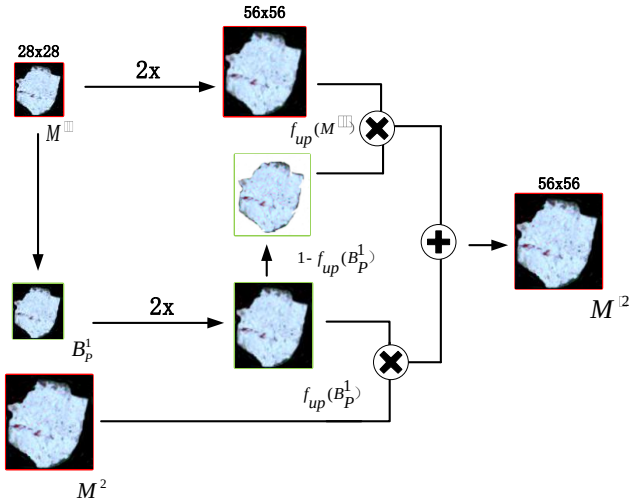

Figure 4. Inference process of Boundary-Aware Refinement

3. Experimental Design

To further verify the impact of the attention mechanism on the accuracy of the improved model to identify and segment quartz, feldspar, lithics and other mineral components, the data set of tight sandstone in Ordos Basin denoised by Gaussian denoising filtering algorithm in irregular region, consisting of 50 images, was used in this experiment. Accurate and precise segmentation results will affect the accuracy of component identification of casting slices. Therefore, two types of experiments, precision experiment and execution speed evaluation, were

designed to comprehensively assess the quality of instance segmentation. The contrast algorithms used in the experiment were YOLACT[29], Mask R-CNN[30], and PointRend[31] (with self-labeling image augmentation mechanism).

The experimental design consists of two parts: accuracy & precision evaluation, and execution speed evaluation. The specific parameters of experimental devices are shown below: CPU: Intel Xeon Silver 4210 R, memory: 64GB, GPU: RTX 6000/8000; operating system: Ubuntu 20.04.3; framework: Tensorflow-GPU 2.1.0. The algorithm used in this paper is based on multi-target instance segmentation, and its principle is similar to that of SLA-RefineMask.

3.1 Accuracy & precision evaluation experiment

To quantitatively evaluate the performance of each model, the following indicators were used for segmentation accuracy evaluation: Precision[32], Recall[33], F1-score[34] and Intersection over Union (IoU)[35]. The identification accuracy of the models was evaluated by calculating precision and recall. Precision represents the proportion of the actual true component in the pixels of tight oil sandstone slice component predicted by the model; Recall indicates the proportion of correctly predicted slice components in the overall slice components. F1-score takes both precision and recall into account to balance the results of precision and recall. IoU measures the degree of overlap between the detected results and the labels, i.e., the degree of overlap between the slice components detected by the model and the slice components in the label. The formulas for calculating each evaluation indicator are represented by Equations (10) - (13).

$$\text{precision} = \frac{\text{TP}}{\text{TP} + \text{FP}} \tag{10}$$

$$\text{Recall} = \frac{\text{TP}}{\text{TP} + \text{FN}} \tag{11}$$

$$F1 = \frac{2 \times \text{Precision} \times \text{Recall}}{\text{Precision} + \text{Recall}} \tag{12}$$

$$\text{IoU} = \frac{TP}{TP + FP + PN} \tag{13}$$

3.2 Execution speed evaluation experiment

The performance of RefineMask and SLA-RefineMask models was evaluated through the execution speed experiment. The execution speed evaluation experiment tests the MRT of both algorithms and judges their execution speed in completing identification tasks. The experimental data set consists of 1600 images from the SZS test set of Ordos Basin. The data set selection is shown in Table 1. The execution speed experiment involves testing the MRT values of the algorithms in completing components identification when the data set consists of 200, 400, 600, 800, 1000, 1200, 1400 and 1600 images, respectively. The number of experiments

was 8 times, and the average value of 8 experiments was finally calculated.

Table 1. Efficiency experiment data set selection

The Amount Of Data	Number Of Original Images	Number Of Amplified Images
200	4	196
400	8	392
600	12	588
800	16	784
1000	20	980
1200	24	1174
1400	28	1372
1600	32	1568

4. Experimental Results and Discussion

4.1 Accuracy and precision experimental results

4.1.1 Accuracy evaluation experimental results

The effect comparison of different models on the tight sandstone data set of Ordos Basin is shown in Table 2:

Conclusion 1: The comparison results of various models on the tight sandstone data set of Ordos Basin show that SLA-RefineMask has higher Recall, F1-Score, and IoU values. The IoU and F1-Score reached 60.65% and 85.26% respectively. The improved method achieved a 5.44% increase in F1-Score and a 1.88% increase in IoU compared to the RefineMask method. This phenomenon indicates that the proposed method has higher segmentation accuracy and better detection of slice components, reducing the false negative rate.

Conclusion 2: Although the Mask R-CNN method has a high Precision value, it has the lowest Recall value. This phenomenon suggests that although Mask R-CNN detects slices, it incorrectly classifies a large number of slice components as other components, leading to rough segmentation recall and inaccurate identification.

Table 2. Comparative experimental results of various models on the tight sandstone data set

Methods	Precision%	Recall%	F1%	IoU%
YOLACT	65.26	72.63	71.52	48.51
Mask R-CNN	**76.74**	70.17	74.13	53.45
PointRend	69.58	76.39	69.41	56.23
RefineMask	70.39	79.64	79.82	58.77
SLA-RefineMask	75.71	**83.14**	**85.26**	**60.65**

4.1.2 Precision evaluation experimental results

In the precision evaluation experiment, confusion matrices (as shown in Figure 5), precision and recall (as shown in Figure 6) were established for two models: RefineMask and SLA-RefineMask. The X-axis of the confusion matrix represents the predicted values, while the Y-axis represents the true values.

By analyzing the experimental results, the following conclusions can be drawn:

Conclusion 1: From Figure 5, it can be observed that some quartz and lithics are misclassified as feldspar, and some cemented dissolution pores are misclassified as primary pores. The reasons for these results are mainly threefold: In slice images, (1) there are more quartz and lithics compared to feldspar, and more cemented dissolution pores than primary pores. (2) Under the polarized light microscope, quartz, feldspar and lithics have similar optical properties, as do cemented dissolution pores and primary pores. (3) There may be mislabeling during the data annotation process, leading to low accuracy of model identification.

Conclusion 2: Figure 6 shows that the SLA-RefineMask model has precision and recall rates for the seven mineral components that are not lower than those of the RefineMask model, with the exception of a lower recall rate for quartz. The reasons for these results are mainly: (1) The attention mechanism is introduced into the feature extraction network of the model to improve the feature extraction of mineral components and enhance the identification precision and recall. (2) There are fewer primary pores compared to casting pores, resulting in more primary pores being misidentified as casting pores and a lower recall for primary pores.

Conclusion 3: As can be seen from Figure 6, the identification accuracy of both algorithms is above 80% and relatively stable. However, the overall accuracy of the algorithm used in this paper is above 90%, indicating that the identification accuracy of the SLA-RefineMask method proposed in this paper is higher.

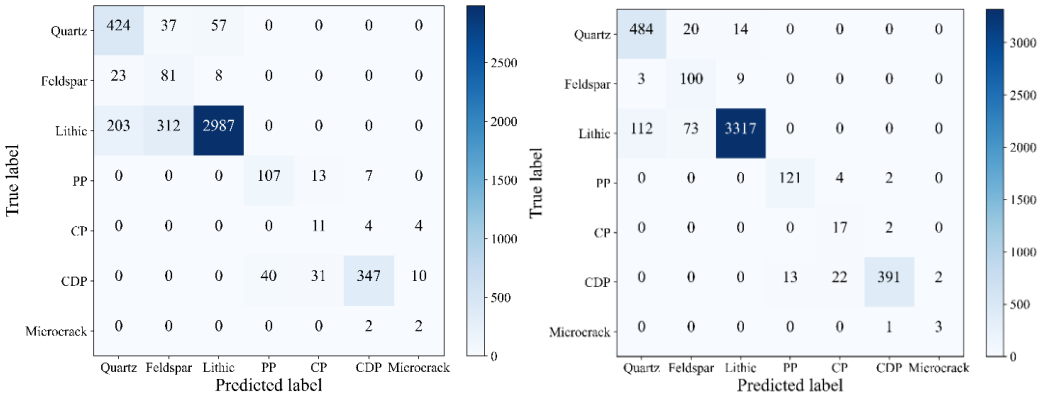

(a)RefineMask model confusion matrix (b)SLA-RefineMask model confusion matrix

Figure 5. Confusion matrix of the two models

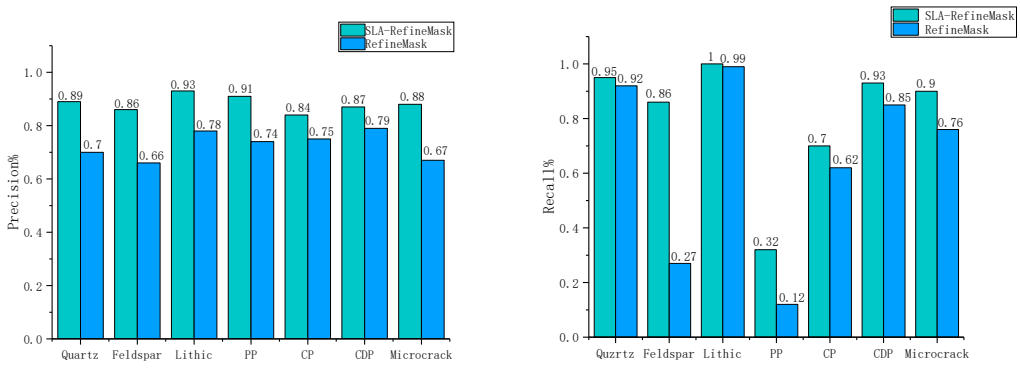

(a) Identification precision of tight sandstone minerals

(b) Identification recall of tight sandstone minerals

Figure 6. Comparison of identification precision and recall of the two models

4.2 Execution speed evaluation experiment

The execution speed experiment results of RefineMask and the proposed algorithm (SLA-RefineMask) are shown in Table 3. The MRT values increase with the amount of experimental data, as shown in Figure 7.

By analyzing the experimental results, the following conclusions can be drawn:

Conclusion 1: From Table 3, it can be observed that the MRT values of the SLA-RefineMask algorithm are smaller than those of the RefineMask algorithm, indicating that the SLA-RefineMask algorithm has faster execution speed. Furthermore, when the experimental data set size is 1600, the MRT of the SLA-RefineMask algorithm is 95.34 seconds, demonstrating that the SLA-RefineMask algorithm's runtime efficiency can meet the practical requirements of slice image segmentation and identification of tight oil sandstone.

Conclusion 2: As shown in Figure 7, the RefineMask algorithm remains relatively stable with a small data set size. However, when the experimental data set size becomes larger (in this experiment, >600), the MRT value increases significantly, indicating that the algorithm is more affected by the data set size. On the other hand, the relationship between the SLA-RefineMask algorithm and the data set size tends to be linearly correlated, indicating that the execution speed of the algorithm is relatively less affected by the data set size.

Table 3. MRT values of different data sets

Experimental Algorithm	Number of Test Sets(N)	MRT(s)
RefineMask	100	9.08
	200	19.06
	400	40.30
	600	63.58
	800	91.03
	1000	121.32
	1200	158.15
	1400	191.64
	1600	237.41
SLA-RefineMask	100	9.08
	200	18.86
	400	36.68
	600	55.04
	800	74.12
	1000	95.34
	1200	124.79
	1400	157.02
	1600	189.75

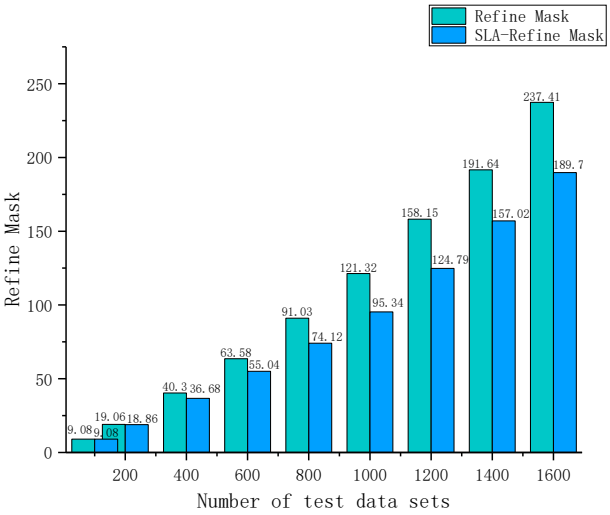

Figure 7. MRT values for different data sets

5. Conclusion

The characterization of slices of tight oil reservoir rocks is a core task in analyzing the micro-pore throat structure, and plays a key role in reservoir sweet spot prediction and micro evaluation. In this paper, the SLA-RefineMask method is proposed to address the problem of low accuracy due to algorithm design flaws, susceptibility to noise interference, sparse sample quantity, etc. Through theoretical exposition and experimental verification, this method can rapidly accomplish the segmentation and identification of slices of tight oil reservoirs with high precision and identification speed. The research conclusions of the SLA-RefineMask method are summarized below:

(1) The use of Gaussian denoising filter algorithm for image preprocessing can effectively improve the image quality and avoid noise interference.

(2) The self-labeling image data augmentation mechanism increases the sample quantity while ensuring sample availability and can increase the sample quantity of the training set. It can effectively alleviate model overfitting and improve model generalization ability.

(3) The SLA-RefineMask algorithm can perform image segmentation and identification simultaneously. The segmentation accuracy results have an error within 10% compared to manual calculation results, and the overall identification accuracy is 94.15%. Therefore, it is suitable for the characterization of slices of tight oil sandstone reservoir rocks in practical applications.

In future work, we will apply the Global Attention Mechanism Generative Adversarial Network (GAN) to optimize the rock image augmentation process of tight oil reservoirs, further ensuring the availability of incremental samples. Additionally, we plan to introduce the superpixel clustering algorithm into the improved

SLA-RefineMask algorithm to enhance the identification effect. Furthermore, we intend to apply the SLA-RefineMask method to the analysis of pore throat features and evaluate its potential.

References

[1] Jiang F , Gu Q , Hao H , et al. A method for automatic grain segmentation of multi-angle cross-polarized microscopic images of sandstone[J]. Computers & Geosciences, 2018, 115(JUN.):143-153.

[2] Cai Xiyuan. 2010. Gas accumulation patterns and key exploration techniques of deep gas reservoirs in tight sandstone: an example from gas exploration in the Xujiahe Formation of the western Sichuan Depression, the Sichuan Basin. Oil & Gas Geology, 31(6):707-714.

[3] Zhou Y , Ji Y , Xu L , et al. Controls on reservoir heterogeneity of tight sand oil reservoirs in Upper Triassic Yanchang Formation in Longdong Area, southwest Ordos Basin, China: Implications for reservoir quality prediction and oil accumulation[J]. Marine & Petroleum Geology, 2016, 78:110-135.

[4] Zhang Z, Chen L, Zhang xin. Exploration of Rock Microscopic Identification Mode Based on SVM. Science & Technology Vision. 2095-2457(2019)36-0027-002.

[5] Wang Chunyao, Chen Junzhou, Li Wei. Review on Superpixel Segmentation Algorithms [J]. Application Research of Computers, 2014,31(01):6-12.

[6]Hariharan B,Arbelbez PGirshick R,et al.Simultaneous detection and segmentation[C]//European conference on computer vision. Springer, Cham, 2014: 297.312.

[7] Yang Dandan, Wang Weixing, Liao Yipeng. Rock Particle Image Segmentation on Multi-scale and Normalized Cut [J]. Journal of Sichuan University (Engineering Science Edition), 2015,47(S1):118-124.DOI:10.15961/j.jsuese.2015.s1.020.

[8] LIU Ye, LYU Jintao. Semi-supervised Rock Image Segmentation and Recognition Based on Superpixel [J]. Advanced Engineering Sciences, 2023, 55(2): 171-183. doi: 10.15961/j.jsuese.202200459

[9] Jiang Feng, Gu Qing, Hao Huizhen, et al. Review of Content-Based Image Segmentation Methods [J]. Journal of Software, 2017,28(01):160-183.DOI:10.13328/j.cnki.jos.005136.

[10] Lei Mingfeng, Zhang Yunbo, Wang Weidong, et al. Research on Intelligent Identification Method and Application of Rock Lithology Mask R-CNN [J]. Journal of Railway Science and Engineering, 2022,19(11):3372-3382.DOI:10.19713/j.cnki.43-1423/u.t20211473.

[11] LUO Hui-lan, CHEN Hong-kun. Survey of Object Detection Based on Deep Learning[J]. ACTA ELECTONICA SINICA, 2020, 48(6): 1230-1239 https://doi.org/10.3969/j.issn.0372-2112.2020.06.026

[12] Song Huansheng, Zhang Xiangqing, Zheng Baofeng, et al. Vehicle Target Detection in Complex Scenes Based on Deep Learning Methods [J]. Application Research of Computers, 2018,35(04):1270-1273.

[13]Liu Xiao-Bo, Liu Peng, Cai Zhi-Hua, Qiao Yu-Lin, Wang Ling, Wang Min. Research progress of optical remote sensing image object detection based on deep learning. Acta Automatica Sinica, 2021, 47(9): 2078−2089 doi: 10.16383/j.aas.c190455

[14] Wang Congzhi, Xu Zibi, Ma Xiangyuan, et al. Mask R-CNN and Data Augmentation and Transfer Learning [J]. Chinese Journal of Biomedical Engineering, 2021,40 (04):410-418.

[15] Gang Zhang, Xin Lu, Jingru Tan, Jianmin Li, Zhaoxiang Zhang, Quanquan Li, Xiaolin Hu; Proceedings of the IEEE/CVF Conference on Computer Vision and Pattern Recognition (CVPR), 2021, pp. 6861-6869 [16] Jafar I F, AlNa'mneh R A, Darabkh K A. Efficient improvements on the BDND filtering algorithm for the removal of highdensity impulse noise[J].IEEE Transactions on Image Processing,2013,22(3) :1223-1232

[17] Rajwade A，Rangarajan A,Banerjee A. Image denoising usingthe higher order singular value decomposition [J].IEEE Transactions on Pattern Analysis and Machine Intelligence,2013,35(4):849-862

[18] Yu Wei, Franchetti F, Hoe J C,et al. Fast bilateral filtering byadapting block size[C] // Proceedings of IEEE InternationalConference on Image Processing. Hong Kong, China, 2010:3281-3284

[19] Si Shaohui, Hu Fuyuan, Gu Yajun, et al. Improved Denoising Algorithm Based on Non-regular Area Gaussian Filtering [J]. Computer Science, 2014,41(11):313-316.

[20] Krizhevsky A., Sutskever I., Hinton G. E., 2012, in Pereira F., Burges C. J. C., Bottou L., Weinberger K. Q., eds, , Advances in Neural Information Processing Systems 25. Curran Associates, Inc., pp 1097–1105.

[21] Dieleman S., Willett K., Dambre J., 2015, MNRAS, 450, 1441.

[22] Li Liangfu, Sun Ruiyun. Bridge Crack Detection Algorithm Based on Image Processing under Complex Background [J]. Laser & Optoelectronics Progress, 2019,56(06):112-122.

[23] Moreno-Barea J , Strazzera F , JM Jerez, et al. Forward Noise Adjustment Scheme for Data Augmentation[C]// IEEE Symposium Series on Computational Intelligence (IEEE SSCI 2018). IEEE, 2018.

[24] Xia Chengjing. Research and Implementation of Facial Expression identification Based on Data Enhancement and CNN [J]. Computer Knowledge and Technology, 2020,16(03):213-215.DOI:10.14004/j.cnki.ckt.2020.0341.

[25] Inoue H . Data Augmentation by Pairing Samples for Images Classification[J]. 2018.

[26] Yang Jin, Li Yuehua, Cao Zhixiang et al. A Hybrid Noise Suppression Method for Passive Millimeter Wave Images [J]. Journal of Microwaves, 2023,39(S1):354-357.

[27] Li L, Fang B, Zhu J. Performance Analysis of the YOLOv4 Algorithm for Pavement Damage Image Detection with Different Embedding Positions of CBAM Modules[J]. Applied Sciences, 2022, 12(19): 10180.

[28] Tsung-Yi Lin, Piotr Dollar, Ross Girshick, Kaiming He,Bharath Hariharan, and Serge Belongie. Feature pyramid networks for object detection. In CVPR, 2017. 1, 2, 3.

[29] Bolya D, Zhou C, Xiao F, et al. Yolact: Real-time instance segmentation[C]//Proceedings of the IEEE/CVF international conference on computer vision. 2019: 9157-9166

[30] He, K., Gkioxari, G., Dollár, P., & Girshick, R. (2017). Mask r-cnn. In Proceedings of the IEEE international conference on computer vision (pp. 2961-2969).

[31] Kirillov, A., Wu, Y., He, K., & Girshick, R. (2020). Pointrend: Image segmentation as rendering. In Proceedings of the IEEE/CVF conference on computer vision and pattern recognition (pp. 9799-9808).

[32] Baeza-Yates R , Ribeiro-Neto B . Modern Information Retrieval: Addison Wesley[J]. Computer Science & Information Technology, 1999.

[33] Liu X , Croft W B . Statistical language modeling for information retrieval[J]. Annual Review of Information Science and Technology, 2006, 39(1):1-31.

[34] Kruitbosch H T , Yasmin M , Sara O , et al. A convolutional neural network for segmentation of yeast cells without manual training annotations[J]. Bioinformatics, 2021(5):5.

[35] Dietler N , Minder M , Gligorovski V , et al. A convolutional neural network segments yeast microscopy images with high accuracy[J]. Nature Communications, 2020, 11(1)